A single inactivating amino acid change in the SARS-CoV-2 NSP3 Mac1 domain attenuates viral replication and pathogenesis *in vivo*

Taha Y. Taha[#, 1], Rahul K. Suryawanshi[#, 1], Irene P. Chen[#, 1, 2], Galen J. Correy[#, 2, 3], Patrick C. O'Leary[2], Manasi P. Jogalekar[2], Maria McCavitt-Malvido[1], Morgan E. Diolaiti[2], Gabriella R. Kimmerly[1], Chia-Lin Tsou[1], Luis Martinez-Sobrido[4], Nevan J. Krogan[2], Alan Ashworth[2]*, James S. Fraser[2, 3]*, Melanie Ott[1, 2, 5]*

[1]Gladstone Institutes, San Francisco, CA 94158
[2]University of California San Francisco, San Francisco, CA 94158
[3]Department of Bioengineering and Therapeutic Sciences, University of California San Francisco, San Francisco, CA 94158
[4]Texas Biomedical Research Institute, San Antonio, TX, 78227, USA
[5]Chan Zuckerberg Biohub – San Francisco, San Francisco, CA 94158

[#]Contributed equally to this work
*Correspondence to: Alan Ashworth (alan.ashworth@ucsf.edu), James S. Fraser (jfraser@fraserlab.com), and Melanie Ott (melanie.ott@gladstone.ucsf.edu)

Abstract

Despite unprecedented efforts, our therapeutic arsenal against SARS-CoV-2 remains limited. The conserved macrodomain 1 (Mac1) in NSP3 is an enzyme exhibiting ADP-ribosylhydrolase activity and a possible drug target. To determine the therapeutic potential of Mac1 inhibition, we generated recombinant viruses and replicons encoding a catalytically inactive NSP3 Mac1 domain by mutating a critical asparagine in the active site. While substitution to alanine (N40A) reduced catalytic activity by ~10-fold, mutations to aspartic acid (N40D) reduced activity by ~100-fold relative to wildtype. Importantly, the N40A mutation rendered Mac1 unstable *in vitro* and lowered expression levels in bacterial and mammalian cells. When incorporated into SARS-CoV-2 molecular clones, the N40D mutant only modestly affected viral fitness in immortalized cell lines, but reduced viral replication in human airway organoids by 10-fold. In mice, N40D replicated at >1000-fold lower levels compared to the wildtype virus while inducing a robust interferon response; all animals infected with the mutant virus survived infection and showed no signs of lung pathology. Our data validate the SARS-CoV-2 NSP3 Mac1 domain as a critical viral pathogenesis factor and a promising target to develop antivirals.

Introduction

The coronavirus disease 2019 (COVID-19) pandemic continues to be a major public health crisis due to the emergence of severe acute respiratory syndrome coronavirus 2 (SARS-CoV-2) variants with enhanced transmissibility and immune escape (1). As of April 2023, more than 760 million people have been infected and more than 6.9 million have died of COVID-19 (2). Despite unprecedented efforts to develop safe and effective vaccines and therapeutics, our arsenal against SARS-CoV-2 remains limited to a few drugs, including remdesivir and molnupiravir targeting the viral RNA-dependent RNA polymerase (RdRp) and nirmatrelvir (ritonavir-boosted as Paxlovid®) targeting the viral NSP5 main protease (MPro). While each of these drugs have shown efficacy in clinical studies (3-5), each is associated with certain drawbacks such as administration via intravenous route for remdesivir, rise of mutations with molnupiravir (6) and drug-drug interactions and resistance mutations of Paxlovid (5, 7-9). There is a critical need to develop novel antivirals targeting other viral proteins to facilitate combination, potentially synergistic, therapeutics and minimize development of drug resistance. Therefore, identification and validation of viral proteins other than the RdRp or MPro as therapeutic targets is necessary.

SARS-CoV-2 is a positive-stranded RNA virus in the coronavirdiae family and the betacoronavirus genus, which also includes SARS-CoV, Middle East respiratory syndrome coronavirus (MERS-CoV), and murine hepatitis virus (MHV). The virus encodes several open reading frames including two large polyproteins 1a and 1ab (PP1a and PP1ab). These polyproteins contain 16 non-structural proteins (NSPs) that are essential components of the viral replicase complex. NSP3 is the largest viral protein and contains several domains including three macrodomains: Mac1, Mac2, and Mac3 (10). Macrodomains are ubiquitous in nature across eukaryotes, prokaryotes, and archaea (11). While Mac2 and Mac3 are catalytically inactive, Mac1 can bind ADP-ribosylated protein sidechains and catalyze the hydrolysis of these post-translational marks for a diverse set of protein targets (10, 12-14). Macrodomains are found and conserved in over 150 viruses (11) and are structurally (15) and evolutionarily (16) related to cellular macrodomains, albeit with distinct functions (17). Viral macrodomains play critical roles in the replication of alphaviruses and hepatitis E virus (18, 19). In coronaviruses (CoV), Mac1 within NSP3 is structurally conserved in several betacoronaviruses lineages including lineage A (MHV), lineage B (SARS-CoV and SARS-CoV-2), and lineage C (MERS-CoV) (20) (Suppl Fig. 1). Collectively, the acquisition, conservation, and evolution of viral macrodomains suggests an evolutionarily conserved fitness advantage of these proteins.

The Mac1 of coronaviruses, including SARS-CoV-2, has ADP-ribosylhydrolayse activity *in vitro* (20). ADP-ribosylation is a ubiquitous post-translational modification that is "written" by poly-adenosine diphosphate-ribose polymerases (PARPs) and is associated with a diverse array of biological consequences (reviewed in (21, 22)), including DNA repair, signal transduction pathways, epigenetics and transcription, and many others. Importantly, PARPs have been shown to be important regulators of virus-host interactions and are integrated in many interferon (IFN) signaling pathways (reviewed in (23)). Specifically, PARP7, PARP9, PARP12 and PARP14 directly enhance antiviral innate immune responses (24-26) and are upregulated during MHV infection (27). The acquisition of an ADP-ribosylhydrolase such as Mac1 in SARS-CoV-2 NSP3 can therefore be seen as a means for the virus to "erase" ADP-ribosylation marks and dampen the antiviral innate immune response. Indeed, previous studies in coronaviruses have demonstrated that the NSP3 Mac1 is necessary for pathogenesis and for robust viral replication (28-31).

Previous studies have typically employed a mutant virus where the conserved asparagine residue at position 40 in the Mac1 active site (Suppl. Fig. 1) is mutated to an alanine residue to render NSP3 Mac1 inactive. In MHV, the Mac1-deficient virus replicated to similar levels as the wild-type (WT) virus *in vitro* but was significantly attenuated in primary bone marrow-derived macrophages and in mice (28, 29). Interestingly, infection with Mac1-deficient MHV-A59 (hepatotropic) was associated with reduced IFN induction compared to infection with Mac1-deficient MHV-JHM (neurotropic) which induced higher levels of IFN in mice (28, 29). The difference between two MHV strains that cause distinct disease pathologies indicates an important role in the host cell type in determining the function of the MHV Mac1. Similar experiments were conducted in SARS-CoV and showed comparable results where the mutant virus displayed replication defects only in mice, but not in cell culture models, and was associated with higher induction of IFN (30). Collectively, these studies suggest a critical role for coronavirus NSP3 Mac1 in viral replication that may not be fully recapitulated in immortalized cell lines. SARS-CoV-2 NSP3 Mac1 has ~75% sequence conservation with SARS-CoV (Suppl. Fig. 1) and has been shown to catalyze the hydrolysis of ADP-ribose moieties from a diverse set of targets (13, 20). Recently, Alhammad et al. generated a SARS-CoV-2 Mac1 deletion mutant (ΔOrf1a 1023-1192) and showed that the mutant has significantly attenuated IFN antagonism and replication *in vivo* (32). The role of the NSP3 Mac1 catalytic activity in SARS-CoV-2 replication and pathogenesis remains unknown.

Here, we show that SARS-CoV-2 NSP3 Mac1 is necessary for robust viral replication *in vivo* and is a reasonable target for the development of novel therapeutics. To catalytically inactivate SARS-CoV-2 Mac1, we focused on mutating the conserved asparagine residue at position 40. Biochemical analysis of alanine and aspartic acid mutants at this residue demonstrated that while both mutants lack catalytic activity, the N40A mutant Mac1 is destabilized and inherently unstable in bacterial and mammalian cells. Using reverse genetics, we show that a SARS-CoV-2 replicon containing NSP3 Mac1 N40A mutation is slightly attenuated in cell culture models without affecting IFN induction, while a replicon and infectious virus containing N40D mutation was associated *with* higher IFN induction but shows minimal replicative effects in immortalized cell lines. In primary airway organoids and in mice, the N40D virus is profoundly attenuated demonstrating the same dichotomy of phenotypes between *in vitro* and *in vivo* studies of Mac1-deficient CoVs. Our studies demonstrate that SARS-CoV-2 Mac1 is a critical viral enzyme that supports viral replication and induces pathogenesis *in vivo.*

Results

Residue N40 is critical for the catalytic activity and protein stability of SARS-CoV-2 Mac1

SARS-CoV-2 NSP3 Mac1 is a MacroD-type macrodomain with high structural conservation with other CoV macrodomains despite sequence divergence (Suppl. Fig. 1). To determine the role of Mac1 in SARS-CoV-2 replication, we wanted to generate Mac1 catalytic activity-deficient SARS-CoV-2 through point mutations that abrogate Mac1 catalytic activity. Several conserved residues in the active site (20), especially asparagine 40 (N40), have been utilized in previous studies of CoV to generate such mutant viruses (28-31). Mac1 N40 coordinates the distal ribose moiety in an ADP-ribosylated substrate and is critical for binding and catalytic activity (30, 33). To investigate the structural and functional contribution of N40 to catalytic and binding activity, we generated Mac1 N40A and N40D mutants which are both predicted to disrupt coordination of the distal ribose moiety and therefore significantly inhibit catalytic activity of Mac1. When expressed as an isolated Mac1 domain in bacteria, the soluble yield of N40A mutant was typically 20-fold lower compared with the WT and N40D Mac1 proteins (Fig. 1A). This suggests that the N40A mutant is unstable or fails to fold efficiently. To determine the thermostability of the mutants in the absence or presence of ADP-ribose, we conducted differential scanning fluorimetry (DSF) and found that the N40A mutant unfolds at a significantly lower temperature (34°C) compared with the WT (49°C) and N40D mutant (46°C) (Fig. 1B and C). All variants were significantly stabilized by ADP-ribose, indicating that binding activity is not greatly compromised (Fig. 1B and C). These data indicate that the N40A mutant may have an inherently unstable fold compared to the WT and N40D mutant, which could be responsible for the low stability and expression yield in bacteria. To determine whether this is also the case in mammalian cells, we generated lentiviral mammalian expression vectors of strep-tagged isolated Mac1 domain and transduced A549 lung carcinoma cells. Western blot analysis of transduced cells revealed that the N40A mutant is expressed at significantly lower levels compared with the WT and N40D mutant (Suppl. Fig. 2). Collectively, these data indicate that Mac1 tolerates an N40A mutation poorly, but it can accommodate an N40D mutation. Interestingly, such a profound effect of the N40A mutant on protein stability in the context of the entire NSP3 protein was not observed for SARS-CoV NSP3 Mac1 as it only resulted in only ~16% reduction in NSP3 expression (30), which suggests different physicochemical properties of these proteins despite high structural similarity.

To determine the binding pose of ADP-ribose for the Mac1 N40D mutant, we crystalized the N40D Mac1 mutant protein in the presence of ADP-ribose (Fig. 1D and E). Relative to WT, the ADP-ribose bound conformation is conserved in the mutant, but the terminal dihedral of the D40 side chain is rotated ~80° relative to N40 and therefore does not form a hydrogen bond with the terminal ribose. This rotation is also observed in the apo structure of N40D (Suppl Fig. 3). Interestingly, in the structure of N40D Mac1 protein bound to ADP-ribose, we observe a water molecule (purple sphere labeled W in Fig. 1E) forming a new hydrogen bond to the terminal ribose that mimics the interaction observed to the nitrogen of N40. To determine whether these subtle differences in binding affect Mac1 enzymatic activity, we conducted deMARylation assays with auto ADP-ribosylated PARP10 and the WT and mutant Mac1 proteins (Fig. 1F). We found that all proteins were capable of deMARylation but the N40D mutant had lower deMARylation activity (Fig. 1F). To quantify the catalytic activity of these proteins, we utilized the NudT5/AMP-Glo assay to measure ADP-ribose released by the enzymatic reaction using adjusted substrate concentrations (Fig. 1G). Given the low activity of the mutants, a 10- and 100-fold excess of the N40A and N40D mutants, respectively, was used in the assay relative to the WT Mac1. Relative to WT Mac1 catalytic activity (k_{cat}/K_M = 0.37 μM^{-1} min^{-1}), the N40A mutant had <10% activity (k_{cat}/K_M = 0.029 μM^{-1} min^{-1}), while the N40D mutant had <1% activity (k_{cat}/K_M = 0.0026 μM^{-1} min^{-1}) (Fig. 1G). These data demonstrate that both mutants have significantly reduced Mac1 enzymatic activities with the N40D mutant having 10-fold and

100-fold lower enzymatic activity relative to the N40A mutant and the WT Mac1. Taken together, these data suggest that the Mac1 N40D mutant is a good surrogate for abolishing catalytic activity in a similar manner to an inhibitor, whereas the significant destabilization observed with the N40A mutant may render it difficult to interpret in the context of the multi-domain structure of NSP3.

The Mac1 N40D replicon has reduced ability to suppress innate immune responses in cell culture

Next, we introduced the N40A and N40D mutations into SARS-CoV-2 replicons to determine their impact on viral RNA replication in a rapid and safe manner (34). The replicons express secreted nanoluciferase as a reporter *au lieu* of the spike-coding sequence and can produce single-round infectious particles when supplied with a separate spike expression vector (Fig. 2A). Single-round infectious particles were generated for the ancestral (WA1) replicon and the two Mac1 N40A and N40D mutants. They were used to infect simian Vero cells overexpressing the ACE2 and TMPRSS2 entry factors (VAT) or human Calu3 lung adenocarcinoma cells naturally expressing both factors. We measured secreted nanoluciferase in the supernatant, which reflects intracellular viral RNA levels (34). The N40D mutant generated similar luciferase signals to the WT replicon in both VAT and Calu3 cells, while the Mac1 N40A mutant showed an ~10-fold reduction (Fig. 2B). Intracellular RNA was isolated from infected Calu3 cells, and both viral and host RNAs were measured by RT-qPCR. Viral RNA levels corresponded well with luciferase measures (Fig. 2B) with the N40A mutant showing an ~10-fold reduction in RNA levels (Fig. 2C). Measurement of a panel of four cytokines (IFNβ, ISG15, IL-6, and STAT1) demonstrated higher induction in N40D-infected cells, especially levels of IFNβ and IL-6, as compared to WT and N40A (Fig. 2D). No such difference was observed with the N40A replicon despite the slight change in viral replication (Fig. 2D). This result suggests that the modest replication deficit but lack of IFN induction of the N40A replicon could result from the observed Mac1 instability rather than a decrease in catalytic activity (Fig. 1G). Therefore, we prioritized the N40D mutant in subsequent experiment to avoid the confounding destabilizing effect of the N40A mutation on Mac1.

To determine if the observed increase in the IFN response was too weak to suppress the N40D mutant replication, Calu3 cells were treated with varying doses of exogenous IFN gamma (IFNγ) and then infected with single rounds of WT and N40D replicons. This treatment significantly decreased viral RNA levels of N40D, and not WT, at the 10 and 100 ng/μL doses as measured by RT-qPCR (Fig. 2E). At 1000 ng/uL IFNγ, activity of both replicons was suppressed (Fig. 2E). Collectively, these data suggest a modest, but specific, effect of the Mac1 N40D mutation on reversing the suppression of innate immune responses in immortalized cell lines.

The Mac1 N40D infectious virus has a 10-fold replication deficit in human airway organoids

To determine whether the Mac1 catalytic activity plays a role in a full replicative infection cycle, we introduced the Mac1 N40D mutation into a WA1-based infectious clone. The clone was transfected into BHK-21 cells and then rescued and passaged over Vero TMPRSS2 cells to achieve high viral titers. After sequence verification, the plaque morphology of the viruses was determined using Vero TMPRSS2 cells; the WT and the N40D mutant showed similar plaque morphology (Fig. 3A). The viruses were then used to infect Calu3 cells; at 48 hours after infection, particle production was measured by plaque assays while intracellular viral RNA and cytokine expression levels were measured by RT-qPCR. The N40D Mac1 mutant showed modestly (~2-fold) lower particle production and intracellular viral RNA compared with the WT virus suggesting a slightly attenuated phenotype (Fig. 2C and 2D). Similar to the results from replicon experiments, the N40D mutant induced higher levels of IFN as compared to WT virus (Fig. 3D), underscoring the specific effect of this mutation in the viral life cycle.

It is possible that the modest phenotype of the N40D mutant observed in Calu3 cells is due to these cells not fully recapitulating the cellular environment during SARS-CoV-2 infection. Human lung organoids are stem-cell derived multi-cell type 3D structures that have intact IFN signaling and better recapitulate the environment during SARS-COV-2 infection (35, 36). We tested the replicative capacity of the N40D mutant in differentiated human airway organoids (Fig. 3E). While WT and Mac1 N40D mutant viruses produced similar levels of infectious particles at 24 hours post infection, the Mac1 N40D mutant showed ~10-fold lower particle production at 48 and 72 hours post infection (Fig. 4B). This observation supports the model that loss of the IFN antagonism limits viral infection by the mutant virus, especially at later time points after infection, and differs from previous work with SARS-CoV where the Mac1-deficient virus phenotype is apparent early post infection (31). Collectively, this data demonstrate that SARS-CoV-2 Mac1 catalytic activity plays a critical role in viral replication in primary cells that is not fully recapitulated in immortalized cell lines.

SARS-CoV-2 Mac1 N40D mutant is significantly attenuated *in vivo*

To ascertain whether SARS-CoV-2 Mac1 catalytic activity plays a role in viral replication *in vivo*, we intranasally infected mice overexpressing the human ACE2 receptor (K18-hACE2) with WT and Mac1 N40D viruses (Fig 4A). In response to WT viral infection, K18-hACE2 mice typically develop significant weight loss and lowered body temperature and reach the humane endpoint by day 6 post infection due to viral encephalitis (37, 38). In contrast, mice infected with the Mac1 N40D mutant did not experience any changes in weight or body temperature, and all mice survived 6 days post infection (Fig. 4B-D). This data indicate that the SARS-CoV-2 Mac1 catalytic activity plays an essential role in viral pathogenesis *in vivo*.

When viral particle production and tissue viral RNA levels were examined in the lungs, upper respiratory tract, and brain, the Mac1 N40D mutant had slightly higher particle production at 2 days post infection but significantly less 4 days post infection and undetectable levels 6 days post infection in the lungs (Fig. 4E, F). Similar decreases were observed in the upper respiratory tract albeit with overall lower viral particle production and tissue RNA levels as expected (Suppl Fig. 4A and 4B). Notably, no infectious particles were recovered from the brain of animals infected with Mac1 N40D mutant virus, consistent with the 100% survival rate of the infected mice (Suppl Fig. 4C). These data indicate efficient entry and replication early post infection, but significantly faster clearance of the Mac1 N40D virus compared with the WT virus. Lung histology of mice infected with the WT and Mac1 N40D virus showed SARS-CoV-2 infection-related pulmonary pathology (39) at 2 days post-infection characterized by inflammation and thickening of alveolar septa by infiltrating immune cells (Fig. 4G). Interestingly, the lung pathology for the mice infected with the Mac1 N40D virus resolved at 4 days post-infection, while the mice infected with the WT virus had persistent pulmonary pathology (Fig. 4G). These histological observations correlate with the differences in the levels of viral replication observed between the WT and Mac1 N40D virus (Fig. 4E and 4F). These results are also consistent with other coronavirus studies, demonstrating a critical role of the Mac1 domain in viral pathogenesis *in vivo* (28-31).

We also collected lung tissues from WT- and N40D-infected animals and extracted RNA for cytokine analysis by RT-qPCR. We selected several cytokines implicated in SARS-CoV-2 clearance and pathogenesis, including *IFNα and IFN6, ISG15, IL6, TNFa, IFNa4, CXCR4, CCL2, and MX1* (40). At all assayed timepoints, Mac1 N40D viral infection was consistently associated with higher cytokine expression relative to the WT virus (Fig. 4H). The most highly induced gene was *ISG15* at 2 and 4 days post infection, while *IFNa4* was highly induced at day 6 (Fig. 4H). Notably, similar cytokine upregulation was previously observed in SARS-CoV Mac1-deficient virus-infected mice (30). Collectively, these data support the model that the SARS-CoV-2 Mac1 catalytic activity is an important suppressor of the innate immune responses and thus critical for viral replication *in vivo*.

Discussion

The SARS-CoV-2 Mac1 domain represents an attractive drug target due to its catalytic ADP-ribosylhydrolase activity, its conserved structure, and its lack of observed mutations in emerging SARS-CoV-2 variants (41). Here we identify –through biochemical and structural characterization– a single amino acid change within the active site (N40D) that diminishes the catalytic activity to <1% of WT activity while maintaining protein stability. This mutation, when introduced via reverse genetics into fully infectious viral clone or replicons, showed minimal effects on viral replication in immortalized cell lines while modestly inducing the IFN response. However, in primary lung organoids and in mice, we observed profound effects of the N40D mutation on viral replication, innate immunity induction and pathogenesis, demonstrating that Mac1 is a critical virulence factor.

CoV Mac1 contains a conserved structure related to MacroD family of macrodomains (11, 33). Several residues in the active site coordinate the ADP-ribose group and have been shown to be critical for ADP-ribosyl substrate binding and catalysis (27). One of the most critical residues is N40 which makes hydrogen bonds with the terminal ribose hydroxyl group and is conserved in all CoV macrodomains. Here we show that this position within the SARS-CoV-2 Mac1 domain does not tolerate mutation to alanine due to protein instability. These results contrast with SARS-CoV Mac1 where the A mutant appears to only modestly reduces the expression of NSP3 in infected cells (30). While structurally conserved, the SARS-CoV-2 Mac1 sequence diverges by 25% from SARS-CoV, and this sequence difference may endow different physicochemical properties to the SARS-CoV-2 Mac1 domain as compared to other CoVs despite maintaining the ADP ribosylhydrolase activity and a well-conserved structural fold.

The CoV Mac1 catalytic activity has been shown to contribute to the suppression of the innate immune responses during SARS-CoV and MHV-JHM infection (29, 30). Recently, a SARS-CoV-2 mutant lacking Mac1 expression showed significant attenuation *in vivo* and reduced IFN antagonism (32). It is not entirely surprising that immortalized cell lines do not fully recapitulate the phenotype of SARS-CoV-2 WT and Mac1 N40D mutant in primary cells or mice. Previous studies with CoV either found no differences in cell culture cells between the WT and Mac1 catalytic activity-deficient viruses or required the use of *in vivo* models or the screening of several

cell culture systems and primary cells to find a cell type in which differences were apparent (28-30, 32). We used two different cell culture lines frequently used in SARS-CoV-2 research: Vero cells (engineered to overexpress ACE2 and TMPRSS2) and Calu3 cells. Vero cells lack IFN production (42) while Calu3 cells have intact IFN production and induction (43), and SARS-CoV-2 replication is dampened in Calu3 cells vs Vero cells due to this critical difference (44). In neither of these cells, did the N40D mutant show much attenuation, as measured by quantification of viral particle production and intracellular viral RNA. In contrast, in primary human lung organoids and in K18-hACE2 mice, the N40D mutant was strongly attenuated and was associated with higher IFN induction. Our findings are reminiscent of what has been reported for other CoVs, and indicate that immortalized cells lines – even those like Calu3 deemed "IFN-competent" may not fully recapitulate innate immune responses during viral infection. Primary cells or *in vivo* models of infection are needed to fully characterize the functional role of certain viral proteins, including the Mac1 domain, in viral infection.

The N40D mutant virus yielded a dramatic survival phenotype in K18-hACE2 mice with all animals surviving while 100% of mice infected with the WT virus reached the humane endpoint. Infected K18-hACE2 mice usually die because of unnatural ACE2 overexpression on neurons and lethal encephalitis (39, 45). However, no infectious virus was recovered from the brains of animals infected with the N40D mutant, correlating with the attenuated viral titers recovered from the lungs of infected animals. It is possible that the Mac1 domain specifically supports neuronal replication of SARS-CoV-2 or that the IFN response when not effectively counterbalanced by the Mac1 domain's catalytic activity is vigorous in infected neurons similarly to the Mac1-deficient MHV-JHM (neurotropic) which induced higher levels of IFN in mice (28, 29). Interestingly, the N40D mutant replicated slightly higher than the WT virus at 2 days post infection in the lungs of infected mice, which correlated with the lack of significant IFN induction at this timepoint. It is possible that elevated ADP-ribosylation of substrates outside the IFN response may support viral replication before the IFN response becomes effectively induced. Future studies will identify the cellular targets of the Mac1 domain and develop effective inhibitors of its catalytic activity to test as potential SARS-CoV-2 therapeutics.

Materials and Methods

All research conducted in this study complies with all relevant ethical regulations. All experiments conducted with replication-competent viruses were conducted in an approved biosafety level 3 (BSL3) laboratory and experiments were approved by the Institutional Biosafety Committee of the University of California, San Francisco and Gladstone Institutes. All protocols concerning animal use were approved (AN169239-01C) by the Institutional Animal Care and Use Committees at the University of California, San Francisco and Gladstone Institutes and conducted in strict accordance with the National Institutes of Health Guide for the Care and Use of Laboratory Animals.

Cells

BHK-21 and A549 cells were obtained from ATCC and cultured in DMEM (Corning) supplemented with 10% fetal bovine serum (FBS) (GeminiBio), 1x glutamine (Corning), and 1x penicillin-streptomycin (Corning) at 37°C, 5% CO_2. Calu3 cells were obtained from ATCC and cultured in AdvancedMEM (Gibco) supplemented with 2.5% FBS, 1x GlutaMax, and 1x penicillin-streptomycin at 37°C and 5% CO_2. Vero cells stably overexpressing human TMPRSS2 (Vero-TMPRSS2) (gifted from the Whelan lab (46)), were grown in DMEM with 10% FBS, 1x glutamine,1x penicillin-streptomycin at 37°C and 5% CO_2. Vero cells stably co-expressing human ACE2 and TMPRSS2 (Vero-ACE2/TMPRSS2) (gifted from A. Creanga and B. Graham at NIH) were maintained in Dulbecco's Modified Eagle medium (DMEM; Gibco) supplemented with 10% FBS, 100 µg/mL penicillin and streptomycin, and 10 µg/mL of puromycin at 37°C and 5% CO_2.

Plasmids

IDT gBlock gene fragments encoding WT and mutant SARS-CoV-2 Mac1 were cloned into a BamHI- and EcoRI-linearized pLVX-EF1alpha-nCoV2019-nsp13-2xStrep-IRES-Puro (Addgene, 141379) by Gibson Assembly Cloning reaction (NEB, 102715-912). Plasmids were validated by whole plasmid sequencing (Primordium). SARS-CoV-2 replicon and infectious clone plasmids were constructed as described previously (34). Briefly, the N40A and N40D mutants were cloned by utilizing NEB HiFi DNA assembly kit onto the second fragment (W2) of the WA1 genetic background. The mutant plasmids were combined with the remaining nine fragments and assembled into the full BAC plasmid using Golden Gate assembly. The resulting plasmid was then maxiprepped and sequenced using Primordium Labs "Large" whole plasmid sequencing service. The Spike (S) and Nucleocapsid (N) expression vectors were described previously (47).

SARS-CoV-2 replicon assay

The SARS-CoV-2 replicon assay was conducted as described previously (34). Briefly, the pBAC SARS-CoV-2 Δ Spike WT, N40A, or N40D plasmid (1 µg), was transfected into BHK21 cells along with N and S expression vectors (0.5 µg each) in 24-well. The supernatant was replaced with fresh growth medium 12-16 hours post transfection. The supernatant containing single-round infectious particles was collected and 0.45 µm-filtered 72 hours post transfection. The supernatant was subsequently used to infect Vero-ACE2 TMPRSS2 cells (in 96-well plate) or Calu3 cells (in 24-well plate). The medium was refreshed 12-24 hours post infection. To measure luciferase activity, an equal volume of supernatant from transfected cells or infected cells was mixed with Nano-Glo luciferase assay buffer and substrate and analyzed on an Infinite M Plex plate reader (Tecan).

Infectious clone virus rescue

pBAC SARS-CoV-2 WT (WA1) or N40D mutant constructs were directly cotransfected with an N expression vector into BHK21 cells in six-well plate. After 3 days, the supernatant was collected and used to infect Vero TMPRSS2 cells and passaged further to achieve high viral titer. All viruses generated and/or utilized in this study were NGS verified using the ARTIC Network's protocol (48).

SARS-CoV-2 virus culture and plaque assay

SARS-CoV-2 infectious clones were propagated on Vero TMPRSS2 cells, sequence verified, and were stored at -80°C until use. For plaque assays, tissue homogenates and cell culture supernatants were analyzed for viral particle formation for *in vivo* and *in vitro* experiments, respectively. Briefly, Vero-ACE2 TMPRSS2 cells were plated and rested for at least 24 hours. Serial dilutions of inoculate of tissue homogenates or cell culture supernatants were added on to the cells. After the 1-hour absorption period, 2.5% Avicel (Dupont, RC-591) was overlaid. After 72 hours, the overlay was removed, the cells were fixed in 10% formalin for one hour, and stained with crystal violet for visualization of plaque formation.

Real-time quantitative polymerase chain reaction (RT-qPCR)

RNA was extracted from cells, supernatants, or tissue homogenates using RNA-STAT-60 (AMSBIO, CS-110) and the Direct-Zol RNA Miniprep Kit (Zymo Research, R2052). RNA was then reverse-transcribed to cDNA with iScript cDNA Synthesis Kit (Bio-Rad, 1708890). qPCR reaction was performed with cDNA and SYBR Green Master Mix (Thermo Fisher Scientific) using the CFX384 Touch Real-Time PCR Detection System (Bio-Rad). N gene primer sequences are: Forward 5′ AAATTTTGGGGACCAGGAAC 3′; Reverse 5′ TGGCACCTGTGTAGGTCAAC 3′. The tenth fragment of the infectious clone plasmid (34) was used as a standard for N gene quantification by RT-qPCR.

K18-hACE2 mouse infection model

K18-hACE2 mice were obtained from the Jackson Laboratory and housed in a temperature- and humidity-controlled pathogen-free facility with 12-hour light/dark cycle and *ad libitum* access to water and standard laboratory rodent chow. Briefly, the study involved intranasal infection ($1X10^3$ PFU) of 6–8-week-old female K18-hACE2 mice with SARS-CoV-2 WA1 or N40D mutant virus. A total of 15 animals were infected for each virus and euthanized at 2, 4, and 6 days post-infection. The lungs and brains were processed for further analysis of virus replication. Mouse lung tissues were fixed in 4% PFA (47608, Sigma) for 24 hours, washed three times with PBS and stored in 70% ethanol. In brief, tissues were processed and embedded in paraffin, and tissue sections were processed for standard Hematoxylin and Eosin staining at Histowiz, Inc (Brooklyn, NY). The sections were then imaged using Leica Aperio ImageScope.

Cellular infection studies

Calu3 cells were seeded into 12-well plates. Cells were rested for at least 24 hours prior to infection. At the time of infection, medium containing viral inoculum was added on the cells. One hour after addition of inoculum, the medium was replaced with fresh medium. The supernatant and cells were harvested at 48 hours post-infection for downstream analysis.

Mac1 expression and purification

SARS-CoV-2 NSP3 Mac1 ($P4_3$ construct, residues 3-169 (49)) was transformed into BL21(DE3) *E. coli* cells (NEB, C2527H) and grown overnight at 37°C lysogeny broth (LB) agar supplemented with carbenicillin (100 µg/mL). Expression starter cultures inoculated with a single colony (10 mL of LB supplemented with carbenicillin) were grown at 37°C for eight hours and were then used to inoculate large scale cultures (1 L of autoinduction

media ZYM-5052 (50). Each 1 L culture was assembled using the following stocks: 960 mL ZY (10 g/L tryptone, 5 g/L yeast extract, prepared in water and autoclaved), 2 mL $MgSO_4$ (1 mM, prepared in water and autoclaved), 1 mL $FeCl_3$ (0.1 M, prepared in 100 mM HCl and sterile filtered), 20 mL 50xM (1.25 mM Na_2HPO_4, 1.25 mM KH_2PO_4, 2.5 mM NH_4Cl, 0.5 mM Na_2SO_4), 20 mL 50x5052 (250 g/L glycerol, 25 g/L glucose, 100 g/L lactose monohydrate, prepared in water and autoclaved). Cultures were grown at 37°C until an optical density of 1, followed by growth at 20°C for 14 hours. Cells were collected by centrifugation (4000 g, 15 minutes, 4°C) and frozen at –80°C. Mac1 was purified and the His-tag cleaved with Tobacco Etch Virus (TEV) protease following the published protocol (49). The purified protein was frozen in liquid nitrogen and stored at –80°C. Point mutations to Asn40 were introduced using Gibson assembly (51) and proteins were purified similarly to WT, except that the Asn40Ala mutant was frozen at 10 mg/mL.

PARP10 expression and purification

Human PARP10 (catalytic domain, residues 819-1007) with a TEV-cleavable His_6-tag was synthesized by Integrated DNA Technologies and cloned into a pET22b(+) vector using Gibson assembly. Protein was expressed similarly to Mac1, except the large-scale cultures were incubated at 18°C for 14 hours. Cells were resuspended in Ni–nitrilotriacetic acid (NTA) binding buffer (50 mM HEPES (pH 7.5), 500 mM NaCl, 10 mM imidazole, 10% glycerol, and 0.5 mM Tris (2-carboxyethyl) phosphine (TCEP), 0.2% Triton X-100 supplemented with TurboNuclease (5 U/mL; Sigma-Aldrich, T4330)) and lysed by sonication. Cell debris was collected by centrifugation (30,000 g, 30 minutes, 4°C), and the lysate was applied to a 5-mL HisTrap HP column (Cytiva, 17524802). The column was washed with 25 mL of binding buffer followed by 25 mL of 5% Ni-NTA elution buffer (50 mM HEPES (pH 7.5), 500 mM NaCl, 500 mM imidazole, 10% glycerol, and 0.5 mM TCEP) and then the protein was eluted with 100% elution buffer. Eluted protein was diluted to 1.6 mg/mL using TEV reaction buffer (50 mM HEPES (pH 7.5), 150 mM NaCl, 1 mM dithiothreitol (DTT), and 5% glycerol) with recombinantly expressed TEV protease (52) added at a 1:20 mass:mass ratio (Mac1:TEV) giving a total volume of 30 mL. The TEV cleavage reaction was incubated at 4°C for 16 hours in a 30 mL 10 kDa molecular weight cutoff dialysis cassette (ThermoFisher Scientific, 66830) dialyzing against 2 L TEV reaction buffer. Following TEV cleavage, the reaction was filtered (0.2 µm cellulose acetate), diluted to 60 mL using TEV reaction buffer and applied to a HisTrap HP column. The cleaved protein was washed off the column using 100% Ni-NTA binding buffer and further purified by size-exclusion chromatography using a HiLoad 16/600 Superdex 75 pg column (Cytiva, 28989333) equilibrated with SEC buffer (20 mM HEPES (pH 7.5), 300 mM NaCl, 10% glycerol and 0.5 mM TCEP). Protein concentration was determined by absorbance at 280 nm using an extinction coefficient of 13410 M-1 cm-1 calculated using the Protparam server (https://web.expasy.org/protparam/).

PARP10 auto-MARylation and Western blotting

Auto-MARylation of PARP10 was carried with reference to the previously published protocol (53). Purified PARP10 was diluted to 20 µM using MARylation buffer (SEC buffer supplemented with 0.02% Triton X-100 and 200 µM β-NAD+ (Roche, NAD100-RO)). The MARylation reaction was incubated at 37°C for 1.5 hours, before filtering (0.2 µM cellulose acetate), concentration with a 10 kDa MWCO centrifugal concentrator (Amicon, UFC901024) and size-exclusion chromatography using a HiLoad 10/300 Superdex 75 pg column (Cytiva, 17517401) to separate the unreacted β-NAD+ (Suppl Fig. 5). Eluted fractions were concentrated to 4.2 mg/mL before being flash frozen in liquid nitrogen and stored at –80°C. Auto-MARylation of PARP10 was assessed by Western blot using an anti-MAR/PAR-antibody (Cell Signaling, 83732). Aliquots of PARP10 taken before and after reaction with β-NAD+ (70 µM µM, 7.5 µg) were boiled for 5 minutes at 95°C in SDS-PAGE loading dye, then separated by SDS-PAGE (Bio-Rad, 456-9036) and transferred to a nitrocellulose membrane (Bio-Rad, 1704158) using a Trans-Blot Turbo transfer system (Bio-Rad). The membrane was stained with Ponceau S (Cell Signaling, 59803S) before destaining with Tris buffered saline Tween-20 (TBST) and incubation for 1 hour with blocking buffer (TBST with 50 g/L blocking agent (Bio-Rad, 1706404)). The membrane was then incubated with primary antibody for 1 hour (1:1000 dilution in blocking buffer), washed with blocking buffer for 30 minutes, then incubated with secondary antibody for 1 hour (1:10000 dilution in blocking buffer, Cell Signaling, 7074S). The horse-radish peroxidase conjugated to the secondary antibody was detected by incubating the membrane with 2 mL chemiluminescence substrate (Bio-Rad, 1705062) for five minutes and then imaged using a ChemiDoc XRS+ imager (Bio-Rad). To assess the removal of ADP-ribose by Mac1, MARylated PARP10 (70 µM, 7.5 µg)

was incubated with Mac1 (20 µM, 2.2 µg) for 1 hour at room temperature. Reactions were stopped by boiling in SDS-PAGE loading dye and blotting for ADP-ribose as described above.

NUDT5 expression and purification

Human NUDT5 (residues 1-219) was expressed from a pET21b vector containing a 3C-protease cleavage N-terminal His_6 tag (54) using BL21(DE3) *E. coli* cells co-transformed with a pKJE7 plasmid expressing the chaperones DnaK, DnaJ and GrpE (Takara, 3340). Cells were grown overnight at 37°C on lysogeny broth (LB) agar supplemented with carbenicillin (100 µg/mL) and chloramphenicol (25 µg/mL). NUDT5 was expressed using autoinduction media with the same method as PARP10, except that media was supplemented with chloramphenicol (25 µg/mL) and chaperone expression was induced with 0.05% arabinose (5 mL of a 100 g/L stock), added when the cultures were cooled from 37°C to 18°C. To purify NUDT5, cells were resuspended in Ni-NTA binding buffer (50 mM HEPES (pH 7.5), 300 mM NaCl, 10 mM imidazole, 5% glycerol, and 0.5 mM TCEP supplemented with TurboNuclease (5 U/mL)) and lysed by sonication. Cell debris was collected by centrifugation, and the lysate was applied to a 5-mL HisTrap HP column. The column was washed with 25 mL of binding buffer followed by 25 mL of 5% Ni-NTA elution buffer (50 mM HEPES (pH 7.5), 300 mM NaCl, 300 mM imidazole, 5% glycerol, and 0.5 mM TCEP) and then eluted with 100% elution buffer. The wash and elution fractions were combined and concentrated to 12 mL using a 10 kDa centrifugal concentrator and desalted into 3C reaction buffer (150 mM NaCl, 50 mM HEPES (pH 7.5), 5% glycerol and 0.5 mM TCEP) using a HiPrep 26/10 desalting column. The sample was diluted to 1.5 mg/mL, and PreScission protease (Cytiva, 27084301) was added to a concentration of 20 U/mg NUDT5 and the reaction was incubated at 4°C overnight. The sample was further purified by anion exchange (AEX) chromatography using a HiTrap Q HP column (Cytiva, 17115401). First, the salt concentration of the sample was reduced to 100 mM using AEX no-salt buffer (50 mM HEPES (pH 7.5), 5% glycerol, 0.5 mM TCEP). Next, the sample was loaded onto the AEX column pre-equilibrated with AEX low-salt buffer (50 mM HEPES (pH 7.5), 100 mM NaCl, 5% glycerol, 0.5 mM TCEP). Bound protein was eluted with a gradient of 0-to-100% high-salt buffer (50 mM HEPES (pH 7.5), 1 M NaCl, 5% glycerol, 0.5 mM TCEP) over 75 mL. The flow through was concentrated and subjected to size-exclusion chromatography using a HiLoad 16/600 Superdex 200 pg column (Cytiva, 28989335) equilibrated with SEC buffer (20 mM HEPES (pH 7.5), 150 mM NaCl and 5% glycerol) (Suppl Fig. 6). Eluted fractions were concentrated to 4.3 mg/mL before being flash frozen in liquid nitrogen and stored at –80°C. The purified NUDT5 was analyzed by SDS-PAGE and the mass confirmed by LC-MS (Suppl Fig. 6) using a Waters Acquity LC connected to a Waters TQ detector with electrospray ionization. Briefly, NUDT5 was diluted to 10 µM using 150 mM NaCl and 20 mM HEPES (pH 7.5) and then 5 µL was injected onto a C4 column held at 40°C. The sample was separated with an initial wash of 95% solvent A (water with 0.1% formic acid) and 5% solvent B (acetonitrile with 0.1% formic acid) for 1.5 min, followed by a linear gradient to 95% solvent B over 6.5 minutes, and a final wash with 95% solvent B for 2 min. All steps were run at 0.2 mL/min.

PARP10 solution assay

The ADP-ribosyl hydrolase activity of macrodomains was determined using the previously described method (54) with auto-MARylated PARP10 as substrate (53). ADP-ribose produced by Mac1 is hydrolyzed by the NUDT5 phosphodiesterase to AMP, which is detected using the AMP-Glo assay kit (Promega, V5011). The activity of the recombinantly expressed NUDT5 with ADP-ribose was determined by serially diluting NUDT5 from 2 to 0.002 µM using PARP10 reaction buffer (20 mM HEPES pH 7.5, 100 mM NaCl, 10 mM $MgCl_2$, 0.5 mM TCEP). NUDT5 (4 µL, 1 to 0.001 µM final concentration) was added to a white 384-well plate (Corning, 3824), and the reaction was initiated with 40 µM ADP-ribose (4 µL, 20 µM final concentration) (Sigma-Aldrich, A0752). After incubation at room temperature for 1 hour, the AMP concentration was quantified by incubation with AMP-Glo reagent I (8 µL) for 1 hour, followed by incubation with a 1:100 mixture of AMP-Glo reagent II and Kinase-Glo one solution (16 µL) for 1 hour. The plate was spun for 1 minute to remove bubbles, and luminescence was measured using a BioTek Synergy HTX plate reader. Values were corrected by subtracting a no-NUDT5 control and plotted as a function of NUDT5 concentration (Supplementary Fig. 5). To quantify the amount of ADP-ribose generated by Mac1, a standard curve was prepared by serially diluting ADP-ribose from 20 to 0.4 µM using PARP10 reaction buffer. ADP-ribose (4 µL, 10 to 0.2 µM final concentration) was added to a 384-well plate and the reaction was initiated with 200 nM NUDT5 (4 µL, 100 nM final concentration) prepared using PARP10 reaction buffer. After incubation at room temperature for 1 hour, the concentration of AMP was determined as above. The plot of

luminescence as a function of ADP-ribose concentration was non-linear at low concentrations of ADP-ribose, therefore the standard curve was fit with a four-parameter logistic equation by non-linear regression using GraphPad prism (Supplementary Fig. 5).

Next, Mac1 and MARylated PARP10 were titrated to determine the MARylated PARP10 concentration and a suitable concentration of Mac1 to use in activity assays. Although the PARP10 concentration was estimated from absorbance at 280 nM, the concentration of ADP-ribose groups attached to PARP10 can be quantified by measuring the amount of ADP-ribose released upon treatment with excess Mac1. Wild type Mac1 was serially diluted from 4 to 0.004 µM and MARylated PARP10 was serially diluted from 40 to 2.5 µM, both using PARP10 reaction buffer. Mac1 (2 µL, 1 to 0.001 µM final concentration) was added to a 384-well plate along with 400 nM NUDT5 (2 µL, 100 nM final concentration) and the reaction was initiated with the serially diluted PARP10 (4 µL, 20 to 1.25 µM final concentration). After incubation at room temperature for 1 hour, the concentration of AMP was determined as above. Substrate depletion was observed at enzyme concentrations ~100 nM and higher, therefore a Mac1 concentration of 5 nM was selected to ensure that the single measurements of ADP-ribose concentration were taken when product formation was linear with respect to time (e.g. when less than 20% of the total substrate was consumed). The concentration of MARylated PARP10 was determined by converting luminescence values at the highest concentration of Mac1 (1 µM) into ADP-ribose concentration using the standard curve (Supplementary Fig. 5). At this Mac1 concentration, all PARP-10 bound ADP-ribose is hydrolyzed to free ADP-ribose.

To determine the rate of Mac1 catalyzed hydrolysis of MARylated PARP10, a mixture of 10 nM Mac1 and 200 nM NUDT5 (4 µL, final concentration of 5 nM for Mac1 and 100 nM for NUDT5) was added to a 384-well plate. The reaction was initiated by adding serially diluted MARylated PARP10 (4 µL, 3.6 to 0.22 µM final corrected concentration) and the reaction was incubated at room temperature for 1 hour followed by AMP detection as above. Enzyme velocities in RLU/min were converted to nM ADP-ribose/min using the standard curve. The increase in enzyme velocity was linear with respect to substrate concentration, suggesting that the [substrate] << K_M, which is consistent with the previously determined K_M for Mac1 with a PARP10 derived peptide (163 µM). The catalytic efficiency of Mac1 (k_{cat}/K_M) was calculated dividing the slope of the substrate-velocity curve by the enzyme concentration, because at substrate concentration << K_M the hydrolysis reaction is first order with respect to both substrate and enzyme concentration. The activity of the Asn40Asp/Ala mutants with auto-MARylated PARP10 were measured as above, however the enzyme concentrations were adjusted to give similar velocities to 5 nM Mac1 (Asn40Asp = 500 nM, Asn40Ala = 50 nM).

X-ray crystallography

Crystals of the N40D mutant in the $P4_3$ space group were grown at 292 K by microseeding with wild-type $P4_3$ crystals using sitting-drop vapor diffusion as described previously (49). The reservoir solution contained 28% PEG 3000 and 100 mM CHES (pH 9.5). Crystals grew overnight and were vitrified directly in liquid nitrogen without additional cryoprotection. The structure with ADP-ribose bound was obtained by soaking a crystal in a solution of 20 mM ADP-ribose prepared in 32% PEG 3000 and 100 mM CHES (pH 9.5) for two hours at room temperature prior to vitrification in liquid nitrogen. X-ray diffraction data were collected at 100 K using beamline 8.3.1 of the Advanced Light Source. Data collection strategy and statistics are shown in Supplementary Table 1. Phases were obtained by molecular replacement with *Phaser* (55) using a model of apo Mac1 derived from PDB code 7KQO with coordinates randomly shifted by 0.3 Å to remove model bias from the apo structure (56). Refinement of the apo model was performed with *phenix.refine* (57) using default settings and five macrocycles at each step. Water molecules were added automatically in phenix.refine to peaks in the $mF_O–DF_C$ map 3.5 σ or higher. Atomic displacement parameters (ADPs) were refined isotropically in the first two cycles of refinement and anisotropically in the remaining cycles. After three cycles of refinement and model building with *Coot* (58), hydrogens were added with *Reduce* (59) run through *phenix.ready_set*. Hydrogens were refined using a riding model, with their ADPs refined isotropically. The occupancy of all water molecules was refined in the final two stages of refinement. For the dataset obtained from a crystal soaked with 20 mM ADP-ribose, ligand binding was confirmed by inspection of $mF_O–DF_C$ electron density maps, with restraints generated by *phenix.elbow* (60). Refinement statistics are shown in Supplementary Table 1.

Differential scanning fluorimetry (DSF)

DSF experiments were performed according to the previously described protocol (49). Briefly, ADP-ribose was dissolved in H_2O to a final concentration of 200 mM, and serial 1:2 dilutions created a ten-point concentration series from 200 to 0.39 mM. DSF buffer was prepared by diluting SYRPO orange (Thermo Fisher Scientific, S6650) from 5000x to 10x in 50 mM Tris (pH 7.5), 150 mM NaCl, 1 mM EDTA, 1 mM DTT, 0.01% Triton X-100. The ADP-ribose concentration series was then diluted 1:100 with DSF buffer (2 µL + 198 µL DSF buffer) and 10 µL was aliquoted into a 384-well white PCR plate (Axygen, PCR-384-LC480-W-NF) and the plates were incubated in the dark for 20 minutes. Purified Mac1 or buffer was then added to each well (10 µL at 4 µM). Each well had a total of 20 µL that contained 2 µM protein (or buffer only), 5x SYPRO orange and 1 to 0.002 mM ADP-ribose (or water only). Each condition was repeated four times, while the no-ADP-ribose conditions were repeated eight times. The PCR plate was sealed with a Microseal 'B' seal (Bio-Rad, MSB1001) and spun to remove air bubbles. The temperature ramp was performed using a BioRad CFX 384 qPCR instrument with fluorescence monitored using the FRET channel from 25 to 95°C at a rate of 1°C/min. Plots of raw RFU values are shown in Suppl Fig. 7. Tma values were calculated online using DSFworld using fitting model 1 (61).

Generation of A549 Mac1-WT and mutant cell lines

Lentivirus was generated using standard protocols and supernatants were collected at 48 hours post transfection, filtered through a 0.45 µm membrane and added to A549 cells 1:1 in complete media supplemented with 8 µg/mL polybrene. The media was changed after 24 hours and, after 48 hours, media containing 2 µg/mL puromycin was added. Cells were selected for 48 hours and then expanded without further selection.

Western blotting for SARS-CoV-2 Mac1

Cell lysates were prepared in Pierce RIPA Buffer (Thermo Fisher Scientific, 89901) containing protease inhibitor and PhosStop cocktails (Roche, 5892970001 and 4906845001, respectively), separated on an SDS-polyacrylamide gel and transferred to a PVDF membrane and probed. The following primary antibodies and dilutions were used: Strep Tag (Thermo Scientific, MA517282, 1:1000) and β-actin-HRP (Cell Signaling, 5125, 1:2000). Images were captured using the Azure c600 Western Blot Imaging System.

ACKNOWLEDGEMENTS

We thank the Whelan laboratory for providing the Vero cells overexpressing human TMPRSS2 and A. Creanga and B. Graham for the Vero cells overexpressing human ACE2 and TMPRSS2. We acknowledge funding support from the NIH F31 AI164671-01 (IPC) and the NIAID Antiviral Drug Discovery (AViDD) grant U19AI171110. We gratefully acknowledge support from the Roddenberry Foundation, P. and E. Taft and the Pendleton Foundation (MO). MO is a Chan Zuckerberg Biohub – San Francisco Investigator. The NUDT5 expression plasmid was a generous gift from Professor In-Kwon Kim. The synchrotron X-ray diffraction data used to determine Mac1 structures were collected at beamline 8.3.1 of the Advanced Light Source. The ALS, a U.S. DOE Office of Science User Facility under contract no. DE-AC02-05CH11231, is supported in part by the ALS-ENABLE program funded by the NIH, National Institute of General Medical Sciences, grant P30 GM124169-01. We thank Francoise Chanut for editorial feedback on the manuscript.

AUTHOR CONTRIBUTIONS STATEMENT

Conceptualization: TYT. and MO. Investigation: TYT, RKS, IPC, GJC, PCO, MPJ, MMM, MED, GRK. Methodology: TYT, RKS, IPC, GJC, PCO, MPJ, LMS, AA, JSF, and MO. Supervision: NJK, AA, JSF, and MO. Writing: TYT, IPC, GJC, LMS, AA, JSF, and MO.

COMPETING INTERESTS

The authors declare the following competing interests: T.Y.T. and M.O. are inventors on a patent application filed by the Gladstone Institutes that covers the use of pGLUE to generate SARS-CoV-2 infectious clones and replicons. All other authors declare no competing interests. A.A. is a co-founder of Tango Therapeutics, Azkarra Therapeutics, Ovibio Corporation and Kytarro, a member of the board of Cytomx and Cambridge Science Corporation, a member of the scientific advisory board of Genentech, GLAdiator, Circle, Bluestar, Earli, Ambagon, Phoenix Molecular Designs and Trial Library, a consultant for SPARC, ProLynx, GSK and Novartis, receives grant or research support from SPARC and AstraZeneca, and holds patents on the use of PARP inhibitors held jointly with AstraZeneca from which he has benefited financially (and may do so in the future).

References

1. Carabelli AM, Peacock TP, Thorne LG, Harvey WT, Hughes J, Consortium C-GU, Peacock SJ, Barclay WS, de Silva TI, Towers GJ, Robertson DL. SARS-CoV-2 variant biology: immune escape, transmission and fitness. Nat Rev Microbiol. 2023:1-16. Epub 2023/01/19. doi: 10.1038/s41579-022-00841-7. PubMed PMID: 36653446; PMCID: PMC9847462.
2. WHO. WHO Coronavirus (COVID-19) Dashboard: World Health Organization; 2022 [cited 2022 9/17/2022]. Available from: https://covid19.who.int/.
3. Beigel JH, Tomashek KM, Dodd LE, Mehta AK, Zingman BS, Kalil AC, Hohmann E, Chu HY, Luetkemeyer A, Kline S, Lopez de Castilla D, Finberg RW, Dierberg K, Tapson V, Hsieh L, Patterson TF, Paredes R, Sweeney DA, Short WR, Touloumi G, Lye DC, Ohmagari N, Oh MD, Ruiz-Palacios GM, Benfield T, Fatkenheuer G, Kortepeter MG, Atmar RL, Creech CB, Lundgren J, Babiker AG, Pett S, Neaton JD, Burgess TH, Bonnett T, Green M, Makowski M, Osinusi A, Nayak S, Lane HC, Members A-SG. Remdesivir for the Treatment of Covid-19 - Final Report. N Engl J Med. 2020;383(19):1813-26. Epub 2020/05/24. doi: 10.1056/NEJMoa2007764. PubMed PMID: 32445440; PMCID: PMC7262788.
4. Jayk Bernal A, Gomes da Silva MM, Musungaie DB, Kovalchuk E, Gonzalez A, Delos Reyes V, Martin-Quiros A, Caraco Y, Williams-Diaz A, Brown ML, Du J, Pedley A, Assaid C, Strizki J, Grobler JA, Shamsuddin HH, Tipping R, Wan H, Paschke A, Butterton JR, Johnson MG, De Anda C, Group MO-OS. Molnupiravir for Oral Treatment of Covid-19 in Nonhospitalized Patients. N Engl J Med. 2022;386(6):509-20. Epub 2021/12/17. doi: 10.1056/NEJMoa2116044. PubMed PMID: 34914868; PMCID: PMC8693688.
5. Hammond J, Leister-Tebbe H, Gardner A, Abreu P, Bao W, Wisemandle W, Baniecki M, Hendrick VM, Damle B, Simon-Campos A, Pypstra R, Rusnak JM, Investigators E-H. Oral Nirmatrelvir for High-Risk, Nonhospitalized Adults with Covid-19. N Engl J Med. 2022;386(15):1397-408. Epub 2022/02/17. doi: 10.1056/NEJMoa2118542. PubMed PMID: 35172054; PMCID: PMC8908851.
6. Theo Sanderson RH, l'ah Donovan-Banfield, Thomas Peacock, Christopher Ruis. Identification of a molnupiravir-associated mutational signature in SARS-CoV-2 sequencing databases. medRxiv. 2023.
7. Jochmans D, Liu C, Donckers K, Stoycheva A, Boland S, Stevens SK, De Vita C, Vanmechelen B, Maes P, Trüeb B, Ebert N, Thiel V, De Jonghe S, Vangeel L, Bardiot D, Jekle A, Blatt LM, Beigelman L, Symons JA, Raboisson P, Chaltin P, Marchand A, Neyts J, Deval J, Vandyck K. The substitutions L50F, E166A and L167F in SARS-CoV-2 3CLpro are selected by a protease inhibitor in vitro and confer resistance to nirmatrelvir. bioRxiv. 2022.
8. Moghadasi SA, Heilmann E, Moraes SN, Kearns FL, von Laer D, Amaro RE, Harris RS. Transmissible SARS-CoV-2 variants with resistance to clinical protease inhibitors. bioRxiv. 2022.
9. Hu Y, Lewandowski EM, Tan H, Morgan RT, Zhang X, Jacobs LMC, Butler SG, Mongora MV, Choy J, Chen Y, Wang J. Naturally occurring mutations of SARS-CoV-2 main protease confer drug resistance to nirmatrelvir. bioRxiv. 2022.
10. Neuman BW, Joseph JS, Saikatendu KS, Serrano P, Chatterjee A, Johnson MA, Liao L, Klaus JP, Yates JR, 3rd, Wuthrich K, Stevens RC, Buchmeier MJ, Kuhn P. Proteomics analysis unravels the functional repertoire of coronavirus nonstructural protein 3. J Virol. 2008;82(11):5279-94. Epub 2008/03/28. doi: 10.1128/JVI.02631-07. PubMed PMID: 18367524; PMCID: PMC2395186.
11. Rack JG, Perina D, Ahel I. Macrodomains: Structure, Function, Evolution, and Catalytic Activities. Annu Rev Biochem. 2016;85:431-54. Epub 2016/02/05. doi: 10.1146/annurev-biochem-060815-014935. PubMed PMID: 26844395.
12. Li C, Debing Y, Jankevicius G, Neyts J, Ahel I, Coutard B, Canard B. Viral Macro Domains Reverse Protein ADP-Ribosylation. J Virol. 2016;90(19):8478-86. Epub 2016/07/22. doi: 10.1128/JVI.00705-16. PubMed PMID: 27440879; PMCID: PMC5021415.
13. Chea C, Lee DY, Kato J, Ishiwata-Endo H, Moss J. Macrodomain Mac1 of SARS-CoV-2 Nonstructural Protein 3 Hydrolyzes Diverse ADP-ribosylated Substrates. bioRxiv. 2023. Epub 2023/03/23. doi: 10.1101/2023.02.07.527501. PubMed PMID: 36945431; PMCID: PMC10028740.
14. Lei J, Kusov Y, Hilgenfeld R. Nsp3 of coronaviruses: Structures and functions of a large multi-domain protein. Antiviral Res. 2018;149:58-74. Epub 2017/11/13. doi: 10.1016/j.antiviral.2017.11.001. PubMed PMID: 29128390; PMCID: PMC7113668.
15. Malet H, Coutard B, Jamal S, Dutartre H, Papageorgiou N, Neuvonen M, Ahola T, Forrester N, Gould EA, Lafitte D, Ferron F, Lescar J, Gorbalenya AE, de Lamballerie X, Canard B. The crystal structures of Chikungunya and Venezuelan equine encephalitis virus nsP3 macro domains define a conserved adenosine binding pocket. J Virol. 2009;83(13):6534-45. Epub 2009/04/24. doi: 10.1128/JVI.00189-09. PubMed PMID: 19386706; PMCID: PMC2698539.

16. Basta HA, Cleveland SB, Clinton RA, Dimitrov AG, McClure MA. Evolution of teleost fish retroviruses: characterization of new retroviruses with cellular genes. J Virol. 2009;83(19):10152-62. Epub 2009/07/25. doi: 10.1128/JVI.02546-08. PubMed PMID: 19625413; PMCID: PMC2748043.
17. Neuvonen M, Ahola T. Differential activities of cellular and viral macro domain proteins in binding of ADP-ribose metabolites. J Mol Biol. 2009;385(1):212-25. Epub 2008/11/06. doi: 10.1016/j.jmb.2008.10.045. PubMed PMID: 18983849; PMCID: PMC7094737.
18. Parvez MK. The hepatitis E virus ORF1 'X-domain' residues form a putative macrodomain protein/Appr-1''-pase catalytic-site, critical for viral RNA replication. Gene. 2015;566(1):47-53. Epub 2015/04/15. doi: 10.1016/j.gene.2015.04.026. PubMed PMID: 25870943; PMCID: PMC7127128.
19. Neuvonen M, Kazlauskas A, Martikainen M, Hinkkanen A, Ahola T, Saksela K. SH3 domain-mediated recruitment of host cell amphiphysins by alphavirus nsP3 promotes viral RNA replication. PLoS Pathog. 2011;7(11):e1002383. Epub 2011/11/25. doi: 10.1371/journal.ppat.1002383. PubMed PMID: 22114558; PMCID: PMC3219718.
20. Alhammad YMO, Kashipathy MM, Roy A, Gagne JP, McDonald P, Gao P, Nonfoux L, Battaile KP, Johnson DK, Holmstrom ED, Poirier GG, Lovell S, Fehr AR. The SARS-CoV-2 Conserved Macrodomain Is a Mono-ADP-Ribosylhydrolase. J Virol. 2021;95(3). Epub 2020/11/08. doi: 10.1128/JVI.01969-20. PubMed PMID: 33158944; PMCID: PMC7925111.
21. Kraus WL. PARPs and ADP-Ribosylation: 50 Years ... and Counting. Mol Cell. 2015;58(6):902-10. Epub 2015/06/20. doi: 10.1016/j.molcel.2015.06.006. PubMed PMID: 26091339; PMCID: PMC4477203.
22. Hoch NC, Polo LM. ADP-ribosylation: from molecular mechanisms to human disease. Genet Mol Biol. 2019;43(1 suppl 1):e20190075. Epub 2020/01/14. doi: 10.1590/1678-4685-GMB-2019-0075. PubMed PMID: 31930280; PMCID: PMC7198025.
23. Fehr AR, Singh SA, Kerr CM, Mukai S, Higashi H, Aikawa M. The impact of PARPs and ADP-ribosylation on inflammation and host-pathogen interactions. Genes Dev. 2020;34(5-6):341-59. Epub 2020/02/08. doi: 10.1101/gad.334425.119. PubMed PMID: 32029454; PMCID: PMC7050484.
24. Atasheva S, Frolova EI, Frolov I. Interferon-stimulated poly(ADP-Ribose) polymerases are potent inhibitors of cellular translation and virus replication. J Virol. 2014;88(4):2116-30. Epub 2013/12/18. doi: 10.1128/JVI.03443-13. PubMed PMID: 24335297; PMCID: PMC3911523.
25. Iwata H, Goettsch C, Sharma A, Ricchiuto P, Goh WW, Halu A, Yamada I, Yoshida H, Hara T, Wei M, Inoue N, Fukuda D, Mojcher A, Mattson PC, Barabasi AL, Boothby M, Aikawa E, Singh SA, Aikawa M. PARP9 and PARP14 cross-regulate macrophage activation via STAT1 ADP-ribosylation. Nat Commun. 2016;7:12849. Epub 2016/11/01. doi: 10.1038/ncomms12849. PubMed PMID: 27796300; PMCID: PMC5095532.
26. Welsby I, Hutin D, Gueydan C, Kruys V, Rongvaux A, Leo O. PARP12, an interferon-stimulated gene involved in the control of protein translation and inflammation. J Biol Chem. 2014;289(38):26642-57. Epub 2014/08/03. doi: 10.1074/jbc.M114.589515. PubMed PMID: 25086041; PMCID: PMC4176246.
27. Grunewald ME, Chen Y, Kuny C, Maejima T, Lease R, Ferraris D, Aikawa M, Sullivan CS, Perlman S, Fehr AR. The coronavirus macrodomain is required to prevent PARP-mediated inhibition of virus replication and enhancement of IFN expression. PLoS Pathog. 2019;15(5):e1007756. Epub 2019/05/17. doi: 10.1371/journal.ppat.1007756. PubMed PMID: 31095648; PMCID: PMC6521996.
28. Eriksson KK, Cervantes-Barragan L, Ludewig B, Thiel V. Mouse hepatitis virus liver pathology is dependent on ADP-ribose-1''-phosphatase, a viral function conserved in the alpha-like supergroup. J Virol. 2008;82(24):12325-34. Epub 2008/10/17. doi: 10.1128/JVI.02082-08. PubMed PMID: 18922871; PMCID: PMC2593347.
29. Fehr AR, Athmer J, Channappanavar R, Phillips JM, Meyerholz DK, Perlman S. The nsp3 macrodomain promotes virulence in mice with coronavirus-induced encephalitis. J Virol. 2015;89(3):1523-36. Epub 2014/11/28. doi: 10.1128/JVI.02596-14. PubMed PMID: 25428866; PMCID: PMC4300739.
30. Fehr AR, Channappanavar R, Jankevicius G, Fett C, Zhao J, Athmer J, Meyerholz DK, Ahel I, Perlman S. The Conserved Coronavirus Macrodomain Promotes Virulence and Suppresses the Innate Immune Response during Severe Acute Respiratory Syndrome Coronavirus Infection. mBio. 2016;7(6). Epub 2016/12/15. doi: 10.1128/mBio.01721-16. PubMed PMID: 27965448; PMCID: PMC5156301.
31. Kuri T, Eriksson KK, Putics A, Zust R, Snijder EJ, Davidson AD, Siddell SG, Thiel V, Ziebuhr J, Weber F. The ADP-ribose-1''-monophosphatase domains of severe acute respiratory syndrome coronavirus and human coronavirus 229E mediate resistance to antiviral interferon responses. J Gen Virol. 2011;92(Pt 8):1899-905. Epub 2011/04/29. doi: 10.1099/vir.0.031856-0. PubMed PMID: 21525212.
32. Yousef M. Alhammad SP, Roshan Ghimire, Joseph J. O'Connor, Catherine M. Kerr, Jessica J. Pfannenstiel, Debarati Chanda, Caden A. Miller, Robert L. Unckless, Sonia Zuniga, Luis Enjuanes, Sunil More,

Rudragouda Channappanavar, Anthony R. Fehr. SARS-CoV-2 Mac1 is required for IFN antagonism and efficient virus replication in mice. bioRxiv. 2023.
33. Correy GJ, Kneller DW, Phillips G, Pant S, Russi S, Cohen AE, Meigs G, Holton JM, Gahbauer S, Thompson MC, Ashworth A, Coates L, Kovalevsky A, Meilleur F, Fraser JS. The mechanisms of catalysis and ligand binding for the SARS-CoV-2 NSP3 macrodomain from neutron and x-ray diffraction at room temperature. Sci Adv. 2022;8(21):eabo5083. Epub 2022/05/28. doi: 10.1126/sciadv.abo5083. PubMed PMID: 35622909; PMCID: PMC9140965.
34. Taha TY, Chen IP, Hayashi JM, Tabata T, Walcott K, Kimmerly GR, Syed AM, Ciling A, Suryawanshi RK, Martin HS, Bach BH, Tsou CL, Montano M, Khalid MM, Sreekumar BK, Kumar GR, Wyman S, Doudna JA, Ott M. Rapid assembly of SARS-CoV-2 genomes reveals attenuation of the Omicron BA.1 variant through NSP6. bioRxiv. 2023. Epub 2023/02/18. doi: 10.1101/2023.01.31.525914. PubMed PMID: 36798416; PMCID: PMC9934579.
35. Sachs N, Papaspyropoulos A, Zomer-van Ommen DD, Heo I, Bottinger L, Klay D, Weeber F, Huelsz-Prince G, Iakobachvili N, Amatngalim GD, de Ligt J, van Hoeck A, Proost N, Viveen MC, Lyubimova A, Teeven L, Derakhshan S, Korving J, Begthel H, Dekkers JF, Kumawat K, Ramos E, van Oosterhout MF, Offerhaus GJ, Wiener DJ, Olimpio EP, Dijkstra KK, Smit EF, van der Linden M, Jaksani S, van de Ven M, Jonkers J, Rios AC, Voest EE, van Moorsel CH, van der Ent CK, Cuppen E, van Oudenaarden A, Coenjaerts FE, Meyaard L, Bont LJ, Peters PJ, Tans SJ, van Zon JS, Boj SF, Vries RG, Beekman JM, Clevers H. Long-term expanding human airway organoids for disease modeling. EMBO J. 2019;38(4). Epub 2019/01/16. doi: 10.15252/embj.2018100300. PubMed PMID: 30643021; PMCID: PMC6376275.
36. Tindle C, Fuller M, Fonseca A, Taheri S, Ibeawuchi SR, Beutler N, Katkar GD, Claire A, Castillo V, Hernandez M, Russo H, Duran J, Crotty Alexander LE, Tipps A, Lin G, Thistlethwaite PA, Chattopadhyay R, Rogers TF, Sahoo D, Ghosh P, Das S. Adult stem cell-derived complete lung organoid models emulate lung disease in COVID-19. Elife. 2021;10. Epub 2021/09/01. doi: 10.7554/eLife.66417. PubMed PMID: 34463615; PMCID: PMC8463074.
37. Suryawanshi RK, Chen IP, Ma T, Syed AM, Brazer N, Saldhi P, Simoneau CR, Ciling A, Khalid MM, Sreekumar B, Chen PY, Kumar GR, Montano M, Gascon R, Tsou CL, Garcia-Knight MA, Sotomayor-Gonzalez A, Servellita V, Gliwa A, Nguyen J, Silva I, Milbes B, Kojima N, Hess V, Shacreaw M, Lopez L, Brobeck M, Turner F, Soveg FW, George AF, Fang X, Maishan M, Matthay M, Morris MK, Wadford D, Hanson C, Greene WC, Andino R, Spraggon L, Roan NR, Chiu CY, Doudna JA, Ott M. Limited cross-variant immunity from SARS-CoV-2 Omicron without vaccination. Nature. 2022;607(7918):351-5. Epub 2022/05/19. doi: 10.1038/s41586-022-04865-0. PubMed PMID: 35584773; PMCID: PMC9279157 Therapeutics, Intellia Therapeutics and Mammoth Biosciences; a scientific advisory board member of Vertex, Caribou Biosciences, Intellia Therapeutics, eFFECTOR Therapeutics, Scribe Therapeutics, Mammoth Biosciences, Synthego, Algen Biotechnologies, Felix Biosciences, The Column Group and Inari; a director at Johnson & Johnson and Tempus; and has research projects sponsored by Biogen, Pfizer, AppleTree Partners and Roche. C.Y.C. is the director of the UCSF-Abbott Viral Diagnostics and Discovery Study; receives research support from Abbott Laboratories; and also receives support for SARS-CoV-2 research unrelated to this study from Mammoth Biosciences.
38. Oladunni FS, Park JG, Pino PA, Gonzalez O, Akhter A, Allue-Guardia A, Olmo-Fontanez A, Gautam S, Garcia-Vilanova A, Ye C, Chiem K, Headley C, Dwivedi V, Parodi LM, Alfson KJ, Staples HM, Schami A, Garcia JI, Whigham A, Platt RN, 2nd, Gazi M, Martinez J, Chuba C, Earley S, Rodriguez OH, Mdaki SD, Kavelish KN, Escalona R, Hallam CRA, Christie C, Patterson JL, Anderson TJC, Carrion R, Jr., Dick EJ, Jr., Hall-Ursone S, Schlesinger LS, Alvarez X, Kaushal D, Giavedoni LD, Turner J, Martinez-Sobrido L, Torrelles JB. Lethality of SARS-CoV-2 infection in K18 human angiotensin-converting enzyme 2 transgenic mice. Nat Commun. 2020;11(1):6122. Epub 2020/12/02. doi: 10.1038/s41467-020-19891-7. PubMed PMID: 33257679; PMCID: PMC7705712.
39. Yinda CK, Port JR, Bushmaker T, Offei Owusu I, Purushotham JN, Avanzato VA, Fischer RJ, Schulz JE, Holbrook MG, Hebner MJ, Rosenke R, Thomas T, Marzi A, Best SM, de Wit E, Shaia C, van Doremalen N, Munster VJ. K18-hACE2 mice develop respiratory disease resembling severe COVID-19. PLoS Pathog. 2021;17(1):e1009195. Epub 2021/01/20. doi: 10.1371/journal.ppat.1009195. PubMed PMID: 33465158; PMCID: PMC7875348.
40. Ann-Kathrin Reuschl LGT, Matthew V.X. Whelan, Dejan Mesner, Roberta Ragazzini, Giulia Dowgier, Nathasha Bogoda, Jane L. E. Turner, Wilhelm Furnon, Vanessa M. Cowton, Giuditta de Lorenzo, Paola Bonfanti, Massimo Palmarini, Arvind H. Patel, Clare Jolly, Greg. J. Towers. Enhanced innate immune suppression by SARS-CoV-2 Omicron subvariants BA.4 and BA.5. bioRxiv. 2022.

41. Hadfield J, Megill C, Bell SM, Huddleston J, Potter B, Callender C, Sagulenko P, Bedford T, Neher RA. Nextstrain: real-time tracking of pathogen evolution. Bioinformatics. 2018;34(23):4121-3. Epub 2018/05/24. doi: 10.1093/bioinformatics/bty407. PubMed PMID: 29790939; PMCID: PMC6247931.
42. Desmyter J, Melnick JL, Rawls WE. Defectiveness of interferon production and of rubella virus interference in a line of African green monkey kidney cells (Vero). J Virol. 1968;2(10):955-61. Epub 1968/10/01. doi: 10.1128/JVI.2.10.955-961.1968. PubMed PMID: 4302013; PMCID: PMC375423.
43. Menachery VD, Eisfeld AJ, Schafer A, Josset L, Sims AC, Proll S, Fan S, Li C, Neumann G, Tilton SC, Chang J, Gralinski LE, Long C, Green R, Williams CM, Weiss J, Matzke MM, Webb-Robertson BJ, Schepmoes AA, Shukla AK, Metz TO, Smith RD, Waters KM, Katze MG, Kawaoka Y, Baric RS. Pathogenic influenza viruses and coronaviruses utilize similar and contrasting approaches to control interferon-stimulated gene responses. mBio. 2014;5(3):e01174-14. Epub 2014/05/23. doi: 10.1128/mBio.01174-14. PubMed PMID: 24846384; PMCID: PMC4030454.
44. Lokugamage KG, Hage A, de Vries M, Valero-Jimenez AM, Schindewolf C, Dittmann M, Rajsbaum R, Menachery VD. Type I Interferon Susceptibility Distinguishes SARS-CoV-2 from SARS-CoV. J Virol. 2020;94(23). Epub 2020/09/18. doi: 10.1128/JVI.01410-20. PubMed PMID: 32938761; PMCID: PMC7654262.
45. Zheng J, Wong LR, Li K, Verma AK, Ortiz ME, Wohlford-Lenane C, Leidinger MR, Knudson CM, Meyerholz DK, McCray PB, Jr., Perlman S. COVID-19 treatments and pathogenesis including anosmia in K18-hACE2 mice. Nature. 2021;589(7843):603-7. Epub 2020/11/10. doi: 10.1038/s41586-020-2943-z. PubMed PMID: 33166988; PMCID: PMC7855185.
46. Case JB, Rothlauf PW, Chen RE, Liu Z, Zhao H, Kim AS, Bloyet LM, Zeng Q, Tahan S, Droit L, Ilagan MXG, Tartell MA, Amarasinghe G, Henderson JP, Miersch S, Ustav M, Sidhu S, Virgin HW, Wang D, Ding S, Corti D, Theel ES, Fremont DH, Diamond MS, Whelan SPJ. Neutralizing Antibody and Soluble ACE2 Inhibition of a Replication-Competent VSV-SARS-CoV-2 and a Clinical Isolate of SARS-CoV-2. Cell Host Microbe. 2020;28(3):475-85 e5. Epub 2020/08/01. doi: 10.1016/j.chom.2020.06.021. PubMed PMID: 32735849; PMCID: PMC7332453.
47. Syed AM, Taha TY, Tabata T, Chen IP, Ciling A, Khalid MM, Sreekumar B, Chen PY, Hayashi JM, Soczek KM, Ott M, Doudna JA. Rapid assessment of SARS-CoV-2-evolved variants using virus-like particles. Science. 2021;374(6575):1626-32. Epub 2021/11/05. doi: 10.1126/science.abl6184. PubMed PMID: 34735219; PMCID: PMC9005165.
48. Emma Betteridge NP, Keith James, Jillian Durham, Josh Quick. COVID-19 ARTIC v3 Illumina library construction and sequencing protocol - short amplicons (275bp). Protocolsio. doi: dx.doi.org/10.17504/protocols.io.bh4zj8x6.
49. Schuller M, Correy GJ, Gahbauer S, Fearon D, Wu T, Diaz RE, Young ID, Carvalho Martins L, Smith DH, Schulze-Gahmen U, Owens TW, Deshpande I, Merz GE, Thwin AC, Biel JT, Peters JK, Moritz M, Herrera N, Kratochvil HT, Consortium QSB, Aimon A, Bennett JM, Brandao Neto J, Cohen AE, Dias A, Douangamath A, Dunnett L, Fedorov O, Ferla MP, Fuchs MR, Gorrie-Stone TJ, Holton JM, Johnson MG, Krojer T, Meigs G, Powell AJ, Rack JGM, Rangel VL, Russi S, Skyner RE, Smith CA, Soares AS, Wierman JL, Zhu K, O'Brien P, Jura N, Ashworth A, Irwin JJ, Thompson MC, Gestwicki JE, von Delft F, Shoichet BK, Fraser JS, Ahel I. Fragment binding to the Nsp3 macrodomain of SARS-CoV-2 identified through crystallographic screening and computational docking. Sci Adv. 2021;7(16). Epub 2021/04/16. doi: 10.1126/sciadv.abf8711. PubMed PMID: 33853786; PMCID: PMC8046379.
50. Studier FW. Protein production by auto-induction in high density shaking cultures. Protein Expr Purif. 2005;41(1):207-34. Epub 2005/05/26. doi: 10.1016/j.pep.2005.01.016. PubMed PMID: 15915565.
51. Gibson DG, Young L, Chuang RY, Venter JC, Hutchison CA, 3rd, Smith HO. Enzymatic assembly of DNA molecules up to several hundred kilobases. Nat Methods. 2009;6(5):343-5. Epub 2009/04/14. doi: 10.1038/nmeth.1318. PubMed PMID: 19363495.
52. Tropea JE, Cherry S, Waugh DS. Expression and purification of soluble His(6)-tagged TEV protease. Methods Mol Biol. 2009;498:297-307. Epub 2008/11/07. doi: 10.1007/978-1-59745-196-3_19. PubMed PMID: 18988033.
53. Dasovich M, Zhuo J, Goodman JA, Thomas A, McPherson RL, Jayabalan AK, Busa VF, Cheng SJ, Murphy BA, Redinger KR, Alhammad YMO, Fehr AR, Tsukamoto T, Slusher BS, Bosch J, Wei H, Leung AKL. High-Throughput Activity Assay for Screening Inhibitors of the SARS-CoV-2 Mac1 Macrodomain. ACS Chem Biol. 2022;17(1):17-23. Epub 2021/12/15. doi: 10.1021/acschembio.1c00721. PubMed PMID: 34904435; PMCID: PMC8691451.

54. Kasson S, Dharmapriya N, Kim IK. Selective monitoring of the protein-free ADP-ribose released by ADP-ribosylation reversal enzymes. PLoS One. 2021;16(6):e0254022. Epub 2021/07/01. doi: 10.1371/journal.pone.0254022. PubMed PMID: 34191856; PMCID: PMC8244878.
55. McCoy AJ, Grosse-Kunstleve RW, Adams PD, Winn MD, Storoni LC, Read RJ. Phaser crystallographic software. J Appl Crystallogr. 2007;40(Pt 4):658-74. Epub 2007/08/01. doi: 10.1107/S0021889807021206. PubMed PMID: 19461840; PMCID: PMC2483472.
56. Correy GJ, Kneller DW, Phillips G, Pant S, Russi S, Cohen AE, Meigs G, Holton JM, Gahbauer S, Thompson MC, Ashworth A, Coates L, Kovalevsky A, Meilleur F, Fraser JS. The mechanisms of catalysis and ligand binding for the SARS-CoV-2 NSP3 macrodomain from neutron and X-ray diffraction at room temperature. bioRxiv. 2022. Epub 2022/02/17. doi: 10.1101/2022.02.07.479477. PubMed PMID: 35169801; PMCID: PMC8845425.
57. Afonine PV, Grosse-Kunstleve RW, Echols N, Headd JJ, Moriarty NW, Mustyakimov M, Terwilliger TC, Urzhumtsev A, Zwart PH, Adams PD. Towards automated crystallographic structure refinement with phenix.refine. Acta Crystallogr D Biol Crystallogr. 2012;68(Pt 4):352-67. Epub 2012/04/17. doi: 10.1107/S0907444912001308. PubMed PMID: 22505256; PMCID: PMC3322595.
58. Emsley P, Lohkamp B, Scott WG, Cowtan K. Features and development of Coot. Acta Crystallogr D Biol Crystallogr. 2010;66(Pt 4):486-501. Epub 2010/04/13. doi: 10.1107/S0907444910007493. PubMed PMID: 20383002; PMCID: PMC2852313.
59. Word JM, Lovell SC, Richardson JS, Richardson DC. Asparagine and glutamine: using hydrogen atom contacts in the choice of side-chain amide orientation. J Mol Biol. 1999;285(4):1735-47. Epub 1999/01/26. doi: 10.1006/jmbi.1998.2401. PubMed PMID: 9917408.
60. Moriarty NW, Grosse-Kunstleve RW, Adams PD. electronic Ligand Builder and Optimization Workbench (eLBOW): a tool for ligand coordinate and restraint generation. Acta Crystallogr D Biol Crystallogr. 2009;65(Pt 10):1074-80. Epub 2009/09/23. doi: 10.1107/S0907444909029436. PubMed PMID: 19770504; PMCID: PMC2748967.
61. Taia Wu JY, Zachary Gale-Day, Amanda Woo, Arundhati Suresh, Michael Hornsby, Jason E. Gestwicki. Three Essential Resources to Improve Differential Scanning Fluorimetry (DSF) Experiments. bioRxiv. 2020.

Figure 1. Expression and characterization of Mac1 N40A and N40D mutants *in vitro*.

A) Analysis of WT, Asn40Ala (N40A) and Asn40Asp (N40D) soluble expression in BL21(DE3) *E. coli* by size exclusion chromatography (HiLoad 16/600 Superdex 75 pg column) and SDS-PAGE (Coomassie stained).
B) Thermostability of Mac1 mutants determined by differential scanning fluorimetry (DSF). Protein (2 μM) was incubated ± 1 mM ADP-ribose with SYPRO orange (10 μM). Apparent melting temperatures were calculated by DSFworld (61) using fitting model 1. Data is presented as the mean of four replicates.
C) Difference in Tma for Mac1 incubated with ADP-ribose from 2 μM to 1 mM. Data is presented as the mean ± SD of four technical replicates.
D) X-ray crystal structure of ADP-ribose bound to N40D. Difference electron density (mF_O-DF_C map) is shown prior to modeling ADP-ribose (blue mesh contoured at 8 σ).
E) ADP-ribose binding is conserved between WT (teal sticks) and N40D (white sticks). Selected hydrogen bonds are shown for WT (red dashed lines) and N40D (black dashed lines). The D40 side chain is rotated ~80° relative to N40 and therefore does not form a hydrogen bond with the terminal ribose, however, a water molecule (purple sphere labeled W) creates a new hydrogen bond network.
F) Western blot analysis of Mac1 activity with auto-MARylated PARP10 (residues 819-1007). MARylated PARP10 (0.5 μM) was incubated with Mac1 variants (20 μM) for 1 hour at room temperature prior to SDS-PAGE and transfer to nitrocellulose membrane and blotting with anti-MAR/PAR antibody (1:1000 dilution, Cell Signaling, 83732).
G) Kinetic measurements of MARylated PARP10 hydrolysis by Mac1 variants (concentration indicated between parentheses) using NudT5/AMP-Glo to detect ADP-ribose (53, 54). Catalytic efficiency (k_{cat}/K_M) was determined by linear regression using GraphPad Prism. Data is presented as the mean ± SD of three technical replicates.

Figure 2. SARS-CoV-2 replicon with Mac1 N40D mutation fails to suppress antiviral immune response in cells.
A) Experimental workflow of the SARS-CoV-2 replicon system. SARS-CoV-2 WA1 and Mac1 domain mutant replicons were transfected along with a S and N expression vectors into BHK21 cells. At 72 hours post-transfection, the supernatant containing single-round infectious particles is used to infect Vero cells stably expressing ACE2 TMPRSS2 (VAT) and Calu3 cells in the presence or absence of exogenous IFN. At 72 hours post-infection, luciferase activity in the supernatants was used as a readout for viral RNA replication and IFN expression is measured by RT-qPCR.
B) Luciferase readout of infected VAT and Calu3 cells with indicated replicons. Data is presented as mean +/- SD of three biological replicates conducted in triplicate.
C) Intracellular viral RNA (N gene copies) of Calu3 cells in B were measured by RT-qPCR using a standard curve. Data is presented as mean +/- SD of three biological replicates conducted in triplicate.
D) Relative expression of indicated cytokines relative to the -Spike control of Calu3 cells in B was determined by RT-qPCR. Data is presented as mean +/- SD of three biological replicates conducted in triplicate.
E) Calu3 cells were infected with indicated replicons in the presence of indicated IFNγ concentrations. Intracellular viral RNA (N gene copies) was measured by RT-qPCR using a standard curve. Data is presented as mean +/- SD of one biological replicate conducted in triplicate.
***, $p<0.001$; ****, $p<0.0001$ by two-sided Student's T-test

Figure 3. SARS-CoV-2 Mac1 domain N40D mutant is attenuated in human airway organoids.

A) Plaque morphology of indicated viruses in VAT cells. The images were pseudocolored in grayscale to optimize plaque visualization.

B) Viral particle release of infected Calu3 cells with indicated viruses was measured at 48 hours post infection by plaque assay on VAT cells. Data is presented as mean +/- SD of two biological replicates conducted in duplicate.

C) Intracellular viral RNA (N gene copies) of Calu3 cells in B were measured by RT-qPCR using a standard curve. Data is presented as mean +/- SD of two biological replicates conducted in duplicate.

D) Relative levels of ISG15, IFNb, IL6, and STAT1 in Calu3 cells in B relative to uninfected cells was determined by RT-qPCR. Data is presented as mean +/- SD of two biological replicates conducted in duplicate.

E) Experimental workflow of the generation of primary human lung organoids and infection with SARS-CoV-2.

F) Viral particle release of infected primary human lung organoids with indicated viruses was measured at indicated times post infection by plaque assay on VAT cells. Data is presented as mean +/- SD of one biological replicate conducted in triplicate.

*, $p<0.05$; **, $p<0.01$ by two-sided Student's T-test

Figure 4. SARS-CoV-2 Mac1 N40D mutant is attenuated in K18-hACE2 mice.

A) K18-hACE2 mice were infected with 10^3 PFUs of WA1 and WA1 Mac1 N40D viruses intranasally. At 2, 4, and 6 days post-infection, the upper respiratory tract and lung tissues were collected for viral particle measurement by plaque assay (VAT) and viral RNA and cytokine expression analysis by RT-qPCR.

B) Survival curve of mice infected in A.

C) Changes in body weight of mice infected in A. Data are shown as mean ± SD.

D) Changes in body temperature of mice infected in A. Data are shown as mean ± SD.

E) Viral particle abundance in the lungs was measured by plaque assay (VAT). Data is presented as mean +/- SD.

F) Viral RNA levels in the lungs was measured by RT-qPCR using a standard curve. Data is presented as mean +/- SD.

G) Relative levels of IFNb, ISG15, IL6, TNFa, IFNa4, CXCR4, CCL2, and MX1 to GAPDH were determined by RT-qPCR. Data is presented as mean +/- SD.

H) Hematoxylin and eosin staining of lungs of mice infected in A.

*, $p<0.05$; **, $p<0.01$; ***, $p<0.001$; ****, $p<0.0001$ by two-sided Student's T-test

Figure 1

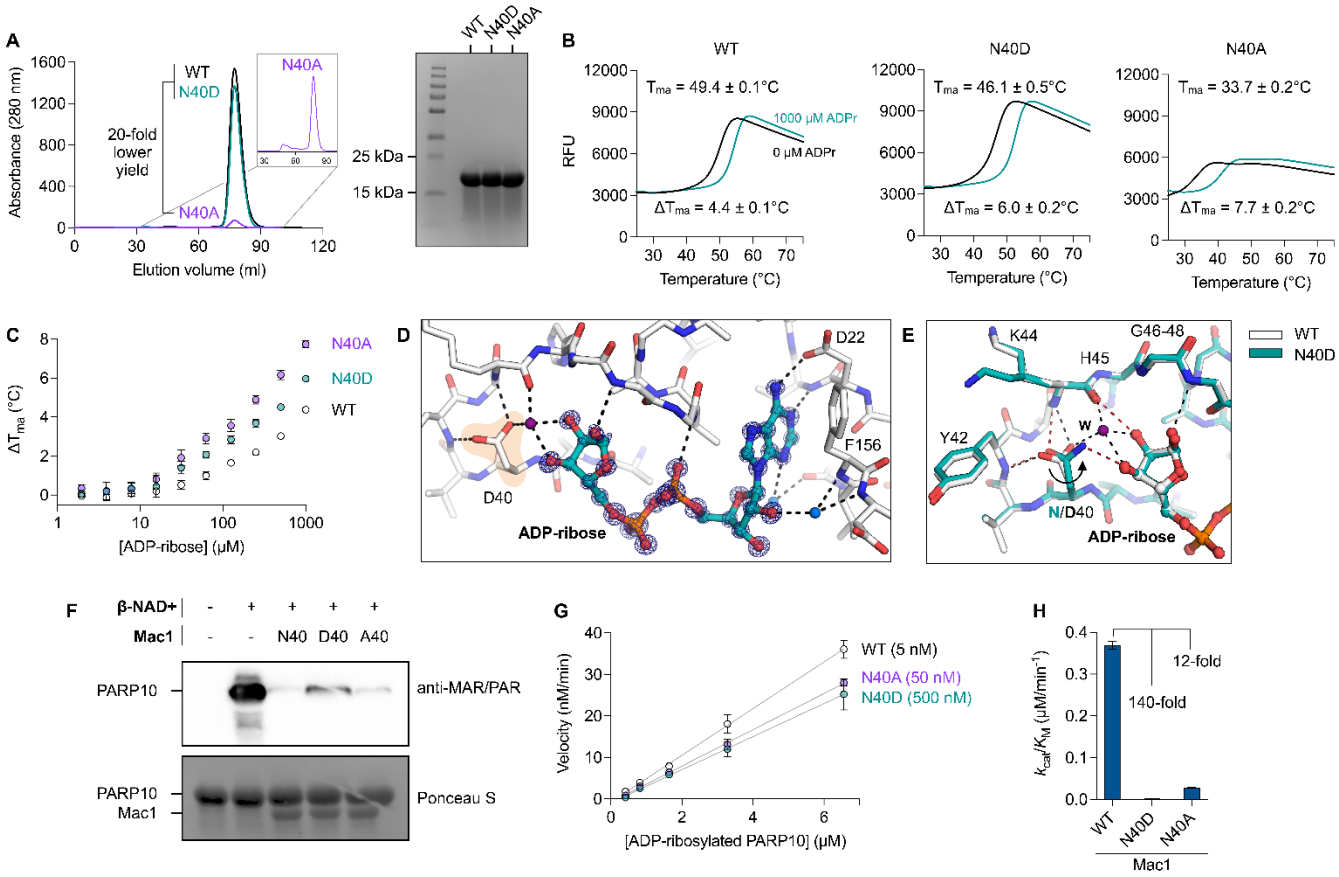

Figure 2

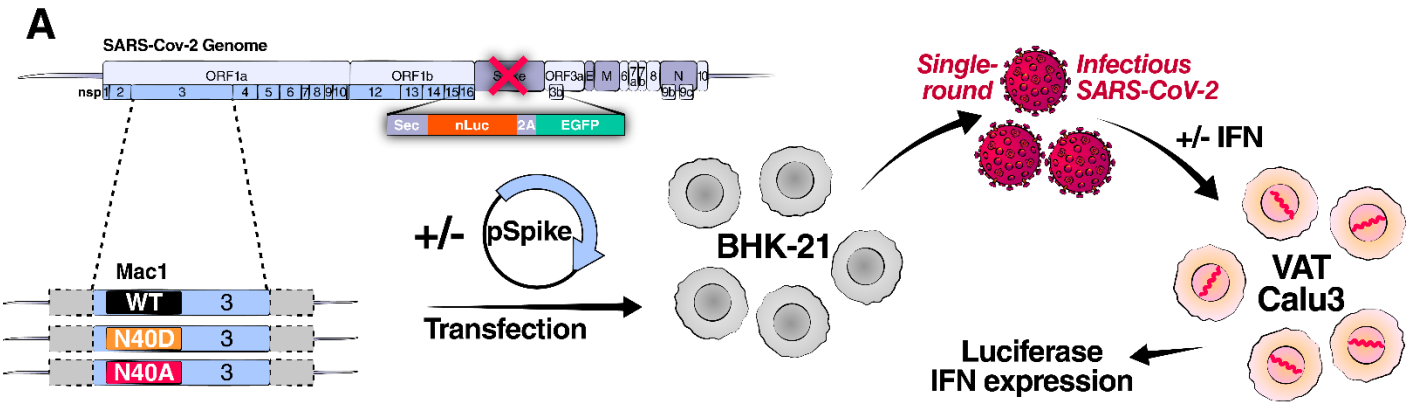

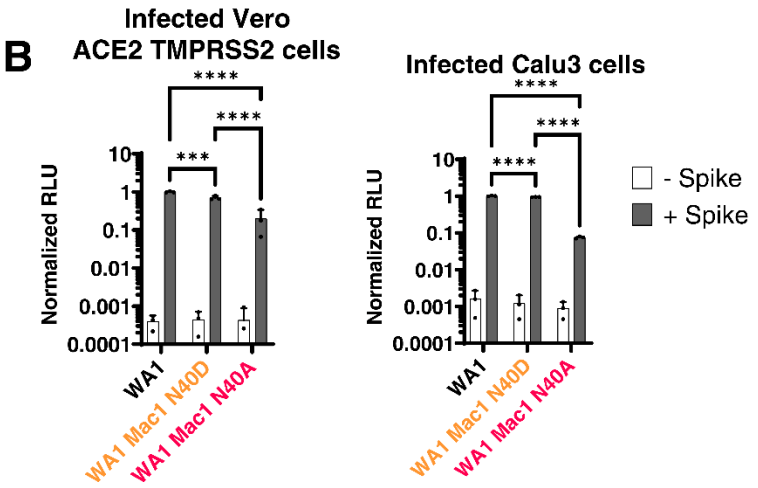

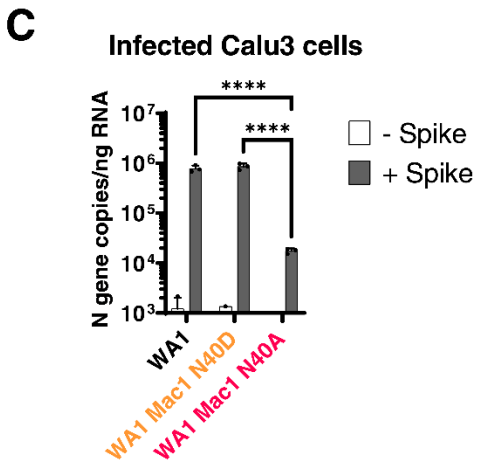

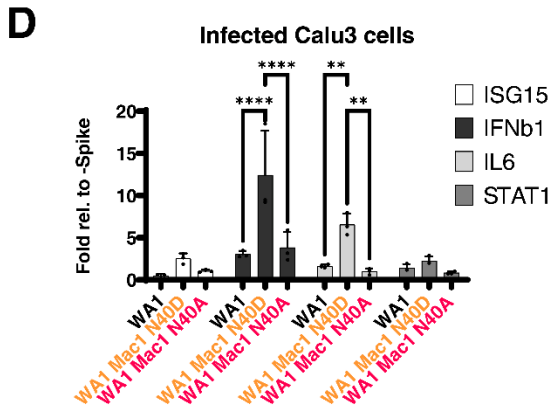

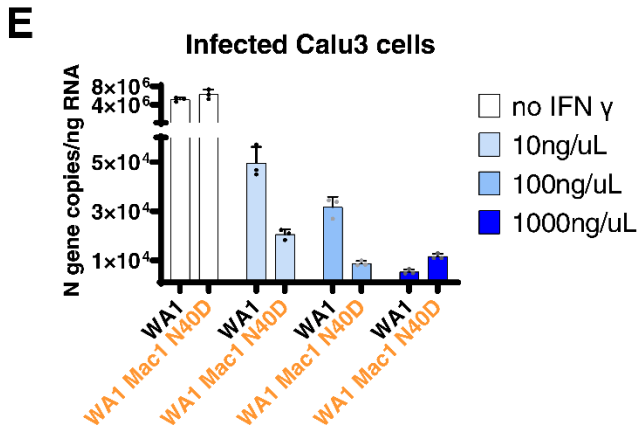

Figure 3

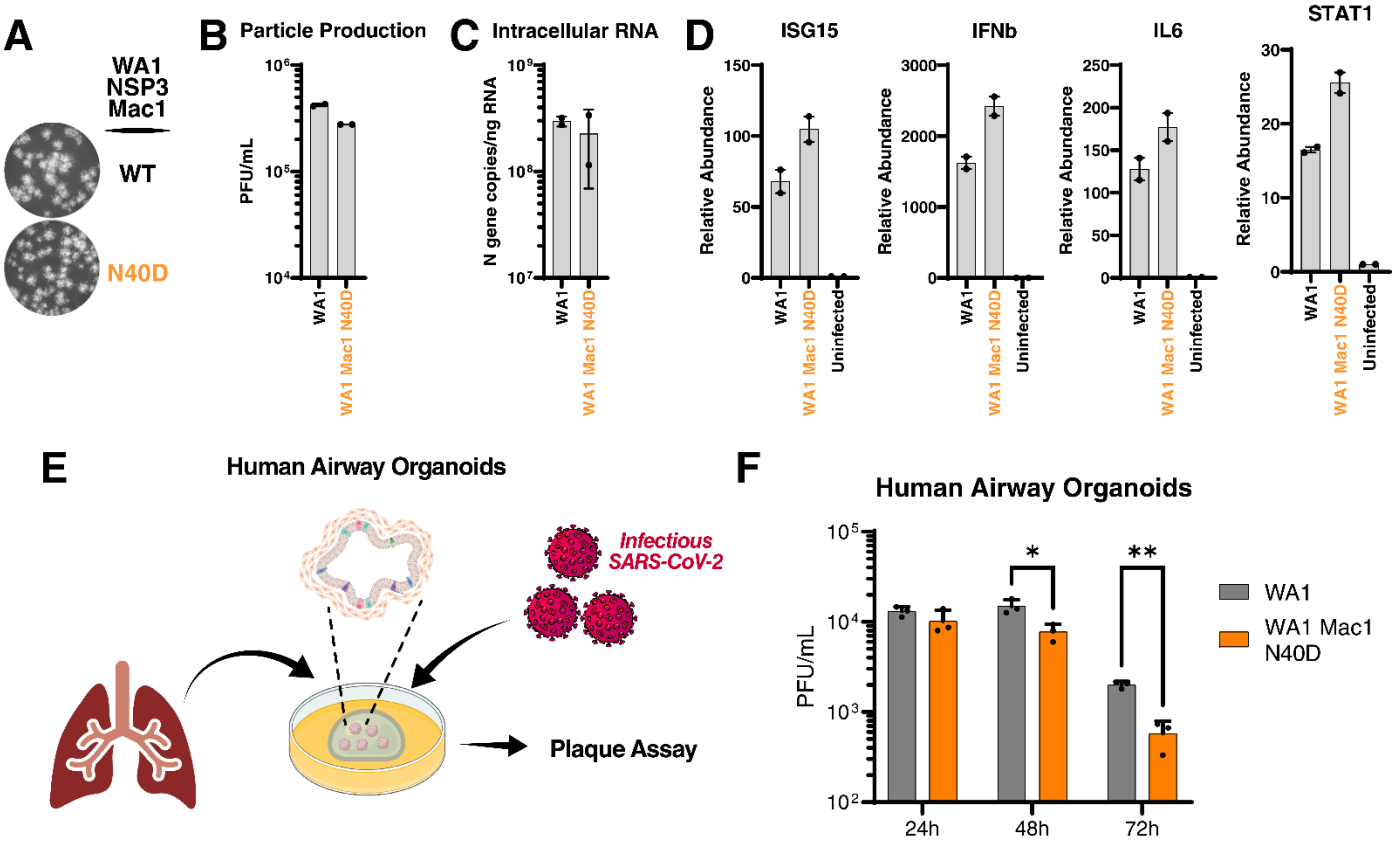

Figure 4